Pergamon

Cement and Concrete Research, Vol. 28, No. 3, pp. 453–463, 1998

0008-8846/98 $19.00 + .00

PII S0008-8846(98)00009-X

MAGNETIC RESONANCE IMAGING AND MOISTURE CONTENT PROFILES OF DRYING CONCRETE

S.D. Beyea,* B.J. Balcom,[1]* T.W. Bremner,† P.J. Prado,* D.P. Green,* R.L. Armstrong,* and P.E. Grattan-Bellew‡

*MRI Centre, Department of Physics, University of New Brunswick, Fredericton, NB, Canada, E3B 5A3

†Materials Group, Department of Civil Engineering, P.O. Box 4400, University of New Brunswick, Fredericton, NB, Canada, E3B 5A3

‡Institute for Research in Construction, National Research Council, Ottawa, ON, Canada, K1A 0R6

(Received August 13, 1997; in final form January 14, 1998)

ABSTRACT

The spatial distribution of moisture in concrete, along with the role this moisture plays in various modes of deterioration, is of fundamental importance to the understanding of concrete behaviour. In this paper a new magnetic resonance imaging technique is utilized for the first time to obtain drying profiles of concrete with sub-millimetre resolution. This technique permits observation of the drying mechanisms, as well as the effects of water-cement ratio and moist curing time on drying behaviour. *© 1998 Elsevier Science Ltd*

Introduction

Moisture has a profound effect on the long-term performance of concrete structures. The moisture content affects strength development and resistance to corrosion, fire, and freeze-thaw (1–6). While not always fully appreciated, the moisture content near the concrete surface is of particular importance. Moisture content varies spatially at the surface of the material due to drying mechanisms, principally capillary flow and molecular diffusion, which are active when concrete is exposed to air (7).

The moisture distribution in the pore structure of the material has both direct and indirect effects. The compressive and tensile strengths of concrete, as well as the modulus of elasticity, are all influenced by moisture content (2). The mechanical strength of concrete will increase as curing progresses only as long as the local relative humidity in the material remains above 80% (8). Drying shrinkage, with concomitant stresses in the weak aggregate/paste interface, leads to the formation of cracks (8). Moist curing followed by drying to a moisture content less than 90% relative humidity aids in freeze-thaw resistance. This is particularly important in concrete that does not contain sufficient air-entrainment (8). When

[1]To whom correspondence should be addressed.

a concrete structure is exposed to fire, explosive spalling will occur if the moisture level is above a critical threshold (4). Corrosion of embedded steel due to chloride ingress is a serious problem as well, especially in bridges and marine structures (9). Corrosion of reinforcement bars only occurs in the presence of both moisture and air. Therefore, both fully dry and fully saturated concrete has a high corrosion resistance (8). In addition, if the permeability of the concrete is decreased, for example by extensive moist curing, the ability of water (and therefore chlorides) to enter the material is decreased.

The ability to predict local moisture content would enable the designer to avoid situations where structural distress is likely to become a problem, or conversely, the concrete could be designed so that it would be resistant to specific field conditions. In order to understand water movement in concrete, a reliable experimental method must be established that can resolve the moisture distribution within the concrete, rapidly, nondestructively, and with sub-millimetre resolution.

While moisture loss in bulk is relatively easy to measure, reliable spatially resolved measurements have proven elusive. Neutron scattering and gamma-ray densimetry have been employed for local moisture content determinations; however the methods are not of general utility (10,11). The gravimetric method with thin sectioning has also been used, but this method is inherently destructive and has poor spatial resolution (7).

Theory

Nuclear magnetic resonance (NMR) has been employed by many groups to study cement chemistry (12–14) and cement pore structure (12,15–18). These classical magnetic resonance methods, principally ^{1}H, do not resolve space but provide a global measure of NMR properties. The NMR relaxation times are sensitive to pore structure and are well known by experiment to decrease as pore size is reduced (18). A variety of theories have been developed to explain why the NMR relaxation times of water in a range of porous materials are influenced by the pore size (19,20). General agreement exists that collision/interaction with the pore walls controls the relaxation behaviour, and the overall relaxation rate will increase with the surface/volume ratio in a pore (15–18).

The relaxation times of interest are the spin lattice relaxation time T_1, the spin spin relaxation time T_2, and the effective spin spin relaxation time T_2^*. The spin lattice relaxation time governs the recovery of longitudinal (parallel to the applied magnetic field) magnetization following excitation with a radio frequency (RF) pulse. The spin spin relaxation time governs the irreversible dephasing of transverse magnetization (perpendicular to the main magnetic field) following a radio frequency pulse. The T_2^* relaxation time describes the effective disappearance of transverse magnetization and incorporates the effects of an inhomogeneous main magnetic field B_0 (21). The T_2^* relaxation time is related to T_2 by Eq. 1:

$$\frac{1}{T_2^*} = \frac{1}{T_2} + \frac{\gamma \cdot \Delta B}{2} \tag{1}$$

where ΔB is the variation in the main magnetic field over the region of interest and γ is the gyromagnetic ratio, an NMR parameter.

Bulk measurements of these relaxation times are of necessity an average over the entire sample. This means, however, that relaxation time studies of pore structure can only be

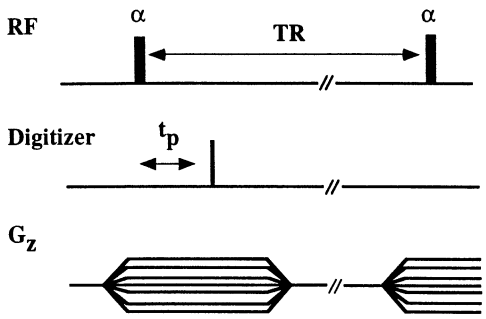

FIG. 1.
Schematic of 1-D SPI method, where α is the RF pulse flip angle, t_p is the encoding time, *TR* is the time between successive RF pulses, and G_z is a magnetic field gradient applied in the *z* direction.

accurately performed on uniformly wet cement samples, as any drying will lead to spatial variations in these properties (22). The case of semi-dry concrete requires a method that is able to resolve space. Ideally the imaging method chosen will retain a sensitivity to the NMR relaxation times.

While best known as a clinical imaging method (23), magnetic resonance imaging (MRI) is increasingly being used to study materials (24). Several groups have attempted to image concrete with clinical MRI methods (25,26). These methods are not suitable for concrete because the relaxation times of water in concrete are several orders of magnitude shorter than relaxation times typically observed in human tissue. McDonald and co-workers have published an MRI study of the invasion of polymer coating material into a deuterated concrete with an MRI method, stray field imaging (STRAFI), which is well suited to the short relaxation times of fluids in concrete (27). They have also very recently employed the STRAFI technique to examine drying behaviour in thin films of silica (28). Kopinga and Pel (29) have developed an NMR instrument for measuring water content in brick materials; however, the method suffers from T_2 relaxation effects and requires a sample-dependent calibration. MRI has been used to observe water displacement through model porous materials (30).

Recently we have demonstrated the use of an MRI method which is ideal for imaging water in concrete samples (31,32). This technique, single point imaging (SPI), does not employ traditional frequency encoding but instead encodes space solely through signal phase (33–35). A schematic of the one-dimensional SPI method is shown in Figure 1. With additional magnetic field gradients, two- and three-dimensional imaging is also possible. In the present study we exploit the cylindrical symmetry of our samples to reduce the experimental problem to one dimension. One-dimensional images of a concrete cylinder yield a profile where the signal intensity at each point in the profile is proportional to the total amount of evaporable water in a plane perpendicular to the long axis of the sample, at a point on this axis, as outlined in Figure 2.

The SPI signal intensity, at any given position, is described by Eq. 2, where ρ(*z*) is the local bulk and/or non-absorbed water content along the *z* direction:

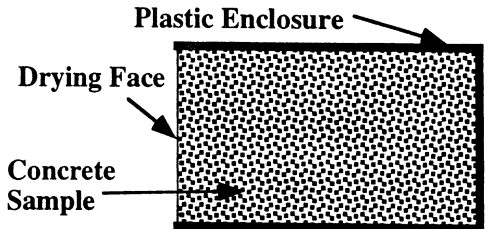

FIG. 2.
Drying concrete in cross section. The imaging axis was parallel to the long axis of the sample. (50 × 70 mm cylinder).

$$S(z) = \rho(z)exp\left(-\frac{t_\rho}{T_2*}\right)\left[\frac{1 - exp\left(-\frac{TR}{T_1}\right)}{1 - cos\alpha \cdot exp\left(\frac{TR}{T_1}\right)} sin\alpha\right] \quad (2)$$

For brief, broadband, RF pulses (small α) and/or repetition times, *TR*, which are much longer than the sample T_1, the signal intensity in the profile is simply proportional to the local water content, weighted by the value of T_2^* at that point and the encoding time, t_p, as shown in Eq. 3:

$$S(z) \propto \rho(z)exp\left(-\frac{t_\rho}{T_2*}\right) \quad (3)$$

If T_2^* is constant at each point on the profile throughout the drying period, then the image is simply proportional to the spatial distribution of evaporable water. If T_2^* is not constant, then the local T_2^* values must be determined, and the profile corrected to extract a true moisture profile. Note that in the SPI experiment we observe primarily liquid phase water sequestered in pores within the concrete medium.

Experimental Details

Sample Preparation

A commercial white Portland cement (Lehigh Portland Cement Co., ASTM Type I, York, PA) and white quartz fine and coarse aggregate (Atlantic Silica Inc., Sussex, NB, Canada) were used in the preparation of the concrete samples because of their low iron content (17). All aggregates were rinsed in distilled water prior to use. Samples were mixed in 5 L batches with water/cement ratios of 0.3, 0.4, 0.5, and 0.6 with a maximum coarse aggregate size of 14 mm (For a description of the properties of the fresh concrete see Table 1). The concrete was then cast into polyethylene vials (50 mm i.d., 100 mm length) and vibrated for 3 s. No air-entrainment was used, but superplasticizer was added to the w/c = 0.3 mix in order to produce a workable mixture. Before casting, the sample containers were soaked in water for 24 h. The concrete specimens were cured for 0, 1, 3, 7, 28, and 90 days in a moist-curing room (relative humidity in excess of 95%, temperature 23 ± 2°C).

TABLE 1
Properties of fresh concrete.

	Series 1	Series 2	Series 3	Series 4
w/c	0.6	0.5	0.4	0.3
Course Agg. (kg/m^3)	888	888	888	888
Fine Agg. (kg/m^3)	868	828	736	582
Slump (mm)	35	30	40	65
Air Content (%)	3.5	2.5	3	3
Unit Weight (kg/m^3)	2230	2310	2340	2700

Samples were cut to 70 mm in length prior to drying (Fig. 2). Individual samples of specified composition and cure time were typically measured at drying times of 0, 1, 3, 7, 30, and 90 days. Samples were dried in an air-conditioned room at 21 ± 2°C and 40 ± 10% relative humidity. During the drying period the samples sat in an open cabinet.

Samples were positioned in a Teflon cradle held in a glass tube, designed to ensure accurate, repetitive placement of the sample within the imaging field of view with minimal background signal. The drying face was positioned in the centre of the image field of view. A Mn(II)-doped water reference was positioned next to the concrete sample to facilitate correction for day to day variations in instrumental sensitivity. Image intensities were scaled by as much as 10% over the course of this 6-month study.

MRI Measurements

The MRI magnet was a Nalorac (Martinez, CA) 2.4 Tesla, 320 mm horizontal-bore superconducting magnet with a water-cooled 20 cm i.d. self-shielded gradient set. All measurements were performed at ambient temperature with a TecMag (Houston, TX) Libra S-16 console, using a home-built birdcage coil driven by a 2 kW AMT (Brea, CA) Model 3445 RF amplifier. The gradient amplifiers were Techron (Elkhart, IN) 7780 amplifiers.

The phase-encoding time, t_p, in the all the MRI experiments shown was 133 μs, while the repetition time, *TR*, was typically 200 ms. The image was encoded by incrementing the *z* gradient in 128 steps to a maximal value of 9 Gauss/cm. Fourier transformation of the phase-encoded signal produced the one-dimensional image profile. Drying profiles had a field of view of 122 mm with a spatial resolution of 0.95 mm, and took 12 min. to acquire with 32 signal averages.

In parallel with the imaging experiments, bulk T_1 and T_2 relaxation times were measured. The T_1 and T_2 relaxation times were frequently multi-exponential. Sample mass (±0.01g) was measured, as a function of drying time with a Mettler PC400 analytical balance.

Discussion of Results

Typical plots of Evaporable Water vs. Position for the concrete drying profiles are shown in Figures 3–5. The y-axis (Evaporable Water) is consistently scaled in all plots to permit sample comparison. The apparent "noise" in the profiles is largely due to local variations in

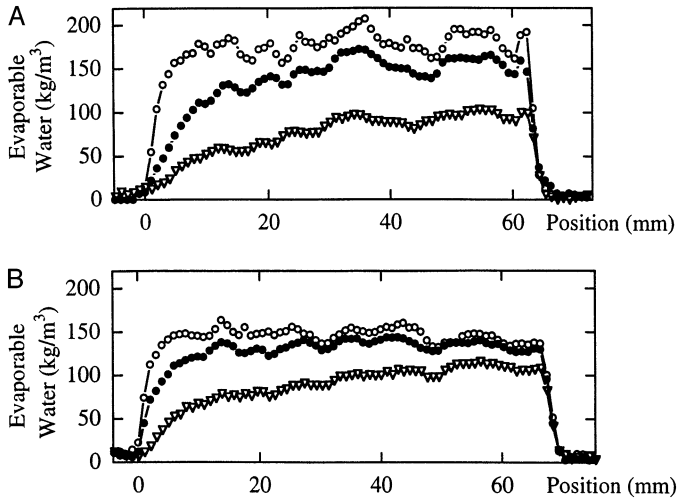

FIG. 3.

A) Drying profiles of concrete with w/c = 0.6 and 1 day of moist curing: profiles shown for 1 (○), 7 (●, and 90 (▽) days of drying. *B*) Drying profiles of concrete with w/c = 0.6 and 90 days of moist curing: profiles shown for 1 (○), 7 (●), and 90 (▽) days of drying.

water content, due to imperfect averaging over the randomly distributed nonporous aggregates.

Samples with a high water-cement ratio and/or short curing times exhibited large amounts of capillary flow at early drying times, as shown by a uniform loss of evaporable water. Diffusive drying fronts were also present at all drying times, but dominated at long drying times. It is impossible, however, to distinguish bulk signal loss due to capillary flow from signal loss due to hydration of the cement grains. Signal from hydrated water decays with a time constant of less than 20 μs and was not observed in these experiments (16).

Samples with extensive moist curing exhibit increased watertightness, as can be shown in both the mass loss curves (Fig. 6) and the drying profiles in Figures 3a and 3b. Samples with longer moist curing periods show large decreases in capillary flow and reduced diffusional water transport. The extended moist curing allows a higher degree of hydration in the concrete. The pore size distributions of the matrix approach smaller dimensions as the capillary pores (cavities found in between the clusters of hydrated products) are replaced by

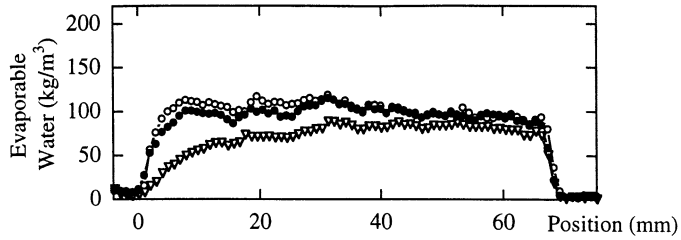

FIG. 4.

Drying profiles of concrete with w/c = 0.5 and 28 days of moist curing: profiles shown for 1 (○), 7 (●), and 90 (▽) days of drying.

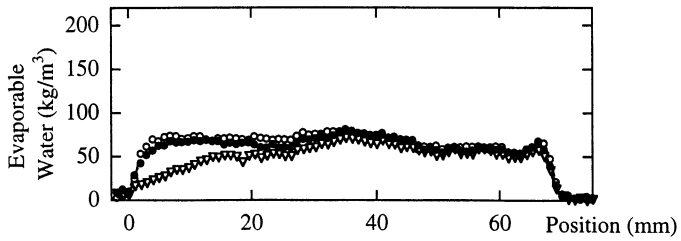

FIG. 5.
Drying profiles of concrete with w/c = 0.3 and 28 days of moist curing: profiles shown for 1 (○), 7 (●), and 90 (▽) days of drying.

gel pores, which results in a densification of the matrix. In addition, the higher degree of hydration results in increased specific surface area of the matrix, which results in a higher moisture retention capacity of the concrete due to increased moisture adsorption (36). The total quantity of evaporable water also decreases. The trend toward reduced average pore size is reflected in the bulk NMR relaxation time data where, for short curing time and/or high water-cement ratio, the average T_1 and T_2 values always decreased with increasing moist-curing time.

The same trends can also be observed with changing water-cement ratio, at constant moist-curing times. An increase in watertightness is apparent in comparing Figures 4 and 5.

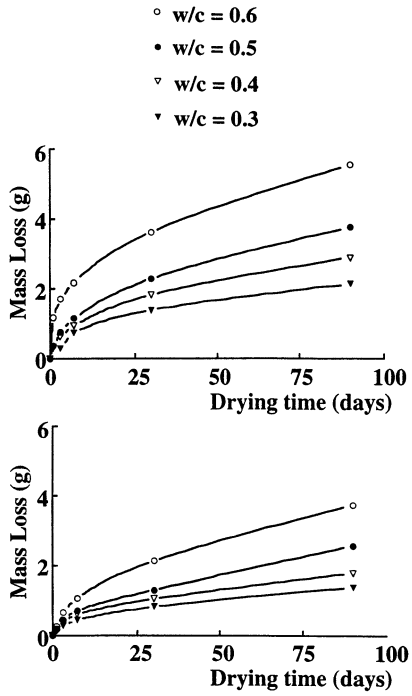

FIG. 6.
Mass of water lost over 90 days of drying for *A*) 1 day of moist curing and *B*) 90 days of moist curing.

Concrete samples with low water-cement ratios (0.3 and 0.4) exhibited little capillary flow compared to those with higher water-cement ratios (0.6 and 0.5), even with moist-curing periods as short as 1 week. Indeed, concrete samples with a low water-cement ratio, and sufficient moist curing, were completely watertight in the interior of the sample, as shown in Figure 5. Samples of this type exhibited no capillary flow and only a small diffusive drying front. This is due to a decrease in porosity/permeability with lower water-cement ratio, and thus a decrease in the number and size of capillary pores within the concrete paste. This was again reflected in the bulk NMR relaxation data where, at curing times of less than 28 days, the average initial T_1 and T_2 values always decreased with decreasing water-to-cement ratio, which again reflects a smaller average pore size.

A comparison of the profiles shows that the drying behaviour of samples with high water-cement ratio but long cure times resembles those of a lower water-cement ratio sample with short cure time. For example, concrete with a water-cement ratio of 0.4 at 90 days of moist curing (not shown) exhibited drying behaviour that closely resembled that of concrete with a water-cement ratio of 0.3 after 28 days of curing. Bulk relaxation data for these samples also resembled each other. This indicates that the pore structure of a concrete with a higher water-cement ratio will be similar to that of a lower water-cement ratio concrete with less curing. Differences in both drying behaviour and bulk relaxation data, which was marked at short curing times, also decreased with curing time.

After 90 days of moist curing, the hydration process is almost completed, yet differences in the drying behaviour still remain. At the end of 90 days of moist curing, the pore structure in the samples is fully formed, with the only differences being the initial amount of mixing water. Thus, concrete with a high water-cement ratio, which does not have sufficient gel volume to fill the original water-filled space, still exhibits significant capillary flow (Fig. 3b). The decrease in capillary flow of high water-cement ratio concrete is then due to a decrease in the average size of the capillary pores, as well as a decrease in the continuity of the capillary system (36). When the water-cement ratio is less than 0.4, the bulk volume of the hydrated gel will completely fill the original water-filled space once the hydration process is complete. This will result in a cement paste free of capillary pores and very low in permeability (8).

The bulk concrete relaxation times were observed to be multi-exponential, with a very long component (T_1 & $T_2 \approx 5$ ms) and two shorter components (T_1 & $T_2 \approx 0.8$ ms, and T_1 & $T_2 \approx 0.16$ ms). The short time component dominated at all times. For samples with a high water-cement ratio, even with 90 days of moist curing, the intermediate relaxation time was seen to decrease with drying, which would seem to be an indication that the larger pores are selectively drying first. Samples with a lower water-cement ratio were seen to have relaxation times that did not change with curing times longer than 3 days. The short component (thought to represent water in the fine gel pores), was constant at all times, but did decrease in amplitude with drying. While it is difficult to accurately fit three exponentials (37), differential scanning calorimetry experiments on similar samples have shown the presence of at least three discrete populations of water with distinct freezing points (38).

If the total signal, for example in Figures 3 to 5, is directly proportional to evaporable water content, then a plot of signal decrease as a function of time, integrated over the entire sample, should be directly proportional to mass loss. These plots for all the water-cement ratios, at all drying times, are linear with drying for the 28 and 90 day moist-cured samples. The plot of mass loss vs. signal loss for these samples is shown as Figure 7b. Similar plots of samples with a shorter moist-curing period demonstrate a characteristic curvature at early

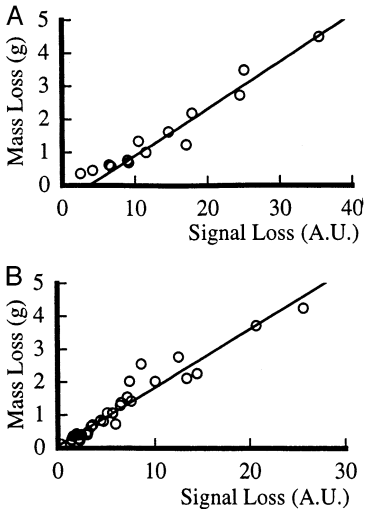

FIG. 7.
Mass loss vs. integrated signal loss for samples with *A*) 0 days moist curing and *B*) 28 and 90 days of moist curing at all water/cement ratios. Mass and signal loss are implicit functions of drying time.

drying times, which is most pronounced for samples with 0 or 1 days of moist curing, as shown in Figure 7a. This is due to the fact that hydration is proceeding at a significant rate throughout the early drying period for the short cure samples (hydration proceeds most rapidly during the first week of curing). When water is bound in cement hydrates it is lost to MRI measurement but does not decrease the mass of the sample, as discussed earlier.

This can be corrected however, if we plot Mass vs. Signal Loss with the initial mass set to the mass of the sample at the end of 7 days from the time of initial preparation, when the rate of curing has significantly decreased. We then obtain linear plots that go through the origin for all samples. This leads to the simple interpretation of the drying profiles shown as being plots of evaporable water. By drying a sample in an oven at 70°C until the mass changed less than 0.01 g in 1 day, and comparing the total signal loss to the total mass loss, we are then able to obtain the calibration of the y-axis for Figures 3 to 5. Drying the samples to "constant mass," and thereby removing all the evaporable water, gave no observable signal, which again supports the conclusion that the signal was simply proportional to evaporable water. In related (unpublished) work (22), we have recently shown that T_2^* in samples of this type does not vary with local water content, which further supports this conclusion (See Eq. 3).

Conclusions

Concrete drying profiles have been obtained, with sub-millimetre resolution and excellent signal-to-noise. Our results indicate that drying occurs through a mixture of capillary and diffusive type flows. Concrete with a water-cement ratio of 0.6 exhibited significant drying, even with 90 days of moist curing. Concrete with a water-cement ratio of 0.3, however, was virtually watertight with curing times as short as 7 days. The true water content profiles will

be compared to current numerical models of drying in an attempt to experimentally validate the models (39).

SPI has been shown to be a sensitive, non-destructive testing method for moisture distribution measurements in concrete. Extensions of the SPI method, and its application to concrete materials, include drying experiments with lightweight concrete, high-speed SPI imaging (31), imaging of the freeze-thaw process (40,41), imaging of salt ingress, and high-resolution three-dimensional imaging of water distribution around porous and non-porous aggregates. We have also recently developed SPI methods to measure local T_1, T_2, and T_2^* relaxation times (22) that will allow us in future experiments to determine the local pore properties using theories of pore relaxation developed for bulk measurements.

Acknowledgments

This work was funded by the NSERC/NRC Research Partnerships program. BJB and RLA acknowledge operating and equipment grants from NSERC of Canada. TWB thanks NSERC's Network of Centre of Excellence and Concrete Canada. We thank Rodney MacGregor and James Merrill for work on the RF probe, Jana Selih for insightful discussions, and Rashmi Pische for her work at the National Research Council, Institute for Research in Construction.

References

1. J.A. Hanson, ACI J. 65, 535 (1968).
2. J.W. Galloway, H.M. Harding, and K.D. Raithby, Effects of Moisture Changes on Flexural and Fatigue Strength of Concrete, Report 864, Transport and Road Research Laboratories, United Kingdom, 1979.
3. R.J. Detwieler, B.J. Dalgleish, and R.B. Williamson, ACI Mater. J. 86, 29 (1989).
4. T.A. Hammer, Marine Concrete Structures Exposed to Hydrocarbon Fire Spalling Resistance of LWA Concrete, Royal Norwegian Council for Scientific and Industrial Research Report, Oslo, Norway, 1990.
5. K. Tuuti, Corrosion of Steel in Concrete, Swedish Cement and Concrete Research Institute, Stockholm, Sweden, 1982.
6. J. Selih, A.C.M. Sousa, and T.W. Bremner, ASCE J. Engng. Mech. 120, 2028 (1994).
7. J. Selih, T.W. Bremner, Mater. Struct. 29, 401 (1994).
8. P.K. Mehta, Concrete Structure, Properties and Materials, Prentice Hall Inc., New Jersey, 1986.
9. T.W. Bremner, Performance of Bridges and Marine Structures in Eastern Canada, International Symposium on Long-Term Observations of Concrete Structures, p. 31, Budapest, 1984.
10. H. Hashida, K. Tanaka, and M. Koike, Build. Res. Pract. 5, 303 (1990).
11. G.E. Monfore, A Review of Methods for Measuring Water Content of Highway Components in Place, Hwy. Res. Rec. 342 (1971).
12. P. Colombet and A.R. Grimmer (eds.) Application of NMR Spectroscopy to Cement Science, Gordon and Breach, Langhorne, PA, 1994.
13. R. Rassem, H. Zanni, J. Lecourtier, J.C. Roussel, and A. Rivereau, Cem. Concr. Res. 23, 1169 (1993).
14. H. Zanni, R. Rassem-Bertolo, S. Masse, L. Fernandez, P. Neito, and B. Bresson, Mag. Reson. Imag. 14, 827 (1996).
15. S. Bhattacharja, M. Moukwa, F. D'Orazio, J-Y. Jehng, and W.P. Halperin, Adv. Cem. Bas. Mater. 1, 67 (1993).
16. W.P. Halperin, J-Y. Jehng, and Y-Q. Song, Mag. Reson. Imag. 12, 169 (1994).

17. R. Blinc, J. Dolinsek, G. Lahajnar, A. Sepe, I. Zupancic, S. Zumer, F. Milia, and M.M. Pintar, Z. Naturforsch 43a, 1026 (1988).
18. E. Laganas, G. Papavassiliou, M. Fardis, A. Leventis, F. Milia, E. Chaniotakis, and C. Meletiou, J. Appl. Phys. 77, 3343 (1995).
19. K.S. Mendelson, W.P. Halperin, J-Y. Jehng, and Y-Q. Song, Mag. Reson. Imag. 12, 207 (1994).
20. B. Sapoval, S. Russ, D. Petit, and J.P. Korb, Mag. Reson. Imag. 14, 863 (1996).
21. P.T. Callaghan, Principles of Nuclear Magnetic Resonance Microscopy, Clarendon Press, Oxford, 1991.
22. S.D. Beyea, B.J. Balcom, P.J. Prado, A.R. Cross, C.B. Kennedy, R.L. Armstrong, and T.W. Bremner, J. Magn. Reson., submitted 1997.
23. D.D. Stark and W.G. Bradley (Eds.), Magnetic Resonance Imaging, C.V. Mosby, St. Louis, 1988.
24. P. Jezzard, J.J. Attard, T.A. Carpenter, and L.D. Hall, Prog. NMR Spectrosc. 23, 1 (1991).
25. J. Link, J. Kaufmann, and K. Schenker, Mag. Reson. Imag. 12, 203 (1994).
26. G. Papavassiliou, F. Milia, M. Fardis, R. Rumm, E. Laganas, O. Jarh, A. Sepe, R. Blinc, and M.M. Pintar, J. Am. Ceram. Soc. 76, 2109 (1993).
27. S. Black, D.M. Lane, P.J. MacDonald, D.J. Hannant, M. Mulheron, G. Hunter, and M.R. Jones, J. Mater. Sci. Lett. 14, 1175 (1995).
28. P.D.M. Hughes, P.J. MacDonald, N.P. Rhodes, J.W. Rockliffe, E.G. Smith, and J. Wills, J. Coll. Interf. Sci. 14, 208 (1996).
29. K. Kopinga and L. Pel, Rev. Sci. Instrum. 65, 3673 (1994).
30. S.N. Sarkar, E.W. Wooten, and R.A. Komoroski, App. Spectrosc. 45, 619 (1991).
31. M. Bogdan, B.J. Balcom, T.W. Bremner, and R.L. Armstrong, J. Magn. Reson. A116, 266 (1995).
32. B.J. Balcom, R.P. MacGregor, S.D. Beyea, D.P. Green, R.L. Armstrong, and T.W. Bremner, J. Magn. Reson. A123, 131 (1996).
33. S. Emid and J.H.N. Creyghton, Physica 128B, 81 (1985).
34. S. Gravina and D.G. Cory, J. Magn. Reson. B104, 53 (1994).
35. D.E. Axelson, A. Kantzas, and T. Eads, Can. J. Appl. Spec. 40, 16 (1995).
36. O.S. Ooi, Aggregate Saturation in Lightweight Concrete. Fredericton, NB, Canada: University of New Brunswick, Ph.D. Thesis. 1988.
37. M. Peyron, G.K. Pierens, A.J. Lucas, L.D. Hall, and R.C. Stewart, J. Magn. Reson. A118, 214 (1996).
38. D.H. Bager and E.J. Sellevold, Cem. Concr. Res. 16, 709 (1986).
39. J. Selih, A.C.M. Sousa and T.W. Bremner, Numerical Simulation of Water Migration in Concrete. Advanced Computational Methods in Heat Transfer II, L.C. Wrobel, C.A. Brebbia, and A.J. Nowak (eds.), Vol. 2, pp. 349–366, Elsevier Applied Science, London, UK, 1992.
40. P.J. Prado, B.J. Balcom, S.D. Beyea, R.L. Armstrong, and T.W. Bremner, Solid State NMR, in press.
41. P.J. Prado, B.J. Balcom, S.D. Beyea, T.W. Bremner, R.L. Armstrong, and P.E. Grattan-Bellew, Cem. Concr. Res., 28, 261 (1998).